Towards real-time self-powered sensing with ample redundant charges by a piezostack-based frequency-converted generator from human motions

Zhongjie Li [a,b,c], Xuzhang Peng [a], Guobiao Hu [d], Dong Zhang [a], Zhibing Xu [a], Yan Peng [b,*], Shaorong Xie [e]

[a] School of Mechatronic Engineering and Automation, Shanghai University, Shanghai 200444, P.R. China
[b] School of Artificial Intelligence, Shanghai University, Shanghai 200444, P.R. China
[c] Engineering Research Center of Unmanned Intelligent Marine Equipment, Ministry of Education, Shanghai 200444, P.R. China
[d] School of Civil and Environmental Engineering, Nanyang Technological University, 50 Nanyang Avenue 639798, Singapore
[e] School of Computer Engineering and Science, Shanghai University, 99 Shangda Rd, Shanghai 200444, P.R. China

ARTICLE INFO

ABSTRACT

This paper presents a piezostack-based frequency up-converting generator for scavenging ultra-low frequency (lower than 5 Hz) vibration energy associated with human motion. The generator, consisting of a force amplifier, a piezoelectric stack, a spring-mass system, and a spring limiter, realizes ultra-low frequency conversion mainly through the impact-induced frequency conversion effect. To estimate the output voltage of the generator numerically, we built a two-degree-of-freedom (2DOF) equivalent model based on the mechanical structure of the harvester. Moreover, we conducted five series of experiments to investigate the output performance of a fabricated prototype. The prototype generates an instantaneous peak-peak output power of 5.56 W (averaged power of 0.93 mW) excited by human running motions. A 'SHU' LED array was lighted up in real-time successfully. We then tested the performance of the prototype in a real-time self-powered system. The generator is able to power a watch and a thermometer in real-time. More importantly, when the excitation stops, they are powered by redundant charges for approximately 50 minutes and 1 minute, respectively. This research can make an essential contribution to ultra-low frequency vibration energy harvesting and the realization of real-time self-powered wearable devices.

1. Introduction

In the past twenty years, with the rapid development of microelectronic technology and the electronic manufacturing industry, portable electronics have been one of the fastest-growing areas of the consumer electronics industry. They are powered mainly by rechargeable chemical batteries, the life span of which is limited. Consequently, more and more attention has been paid to capturing energy from human motions for realizing real-time self-powering functions of wearables without batteries. Mechanical vibration energy is the most abundant energy from human motions. To convert the vibration energy into electricity, three transduction approaches are commonly proposed, namely, electromagnetic [1–8], piezoelectric [9–16], and triboelectric [17–22] mechanisms. The high power density constitutes [23] that a piezoelectric mechanism is a mainstream approach to absorbing energy from human motion.

Many researchers proposed piezoelectric energy harvesters (PEHs) to harvest human kinetic energy to charge energy storage units. Kim *et al.* [24] demonstrated a composite PEH for a smart home with an instantaneous power of 11 mW at a resistance of 165 kΩ. Yuan *et al.* [25] developed a circular PEH which reached a maximum output power of 27 mW at 90 Hz and 2 g excitation under the resistance of 25 kΩ. In addition, some designs combined two different energy harvesting techniques, piezo-triboelectric [26,27] and piezo-electromagnetic [28–30] techniques, for instance. Hamid and Yuce [31] demonstrated an energy harvesting system using a hybrid piezo-electromagnetic mechanism to generate 75.6 μJ with riding a bike under 35–38 km/h. Guo *et al.* [32] reported an all-fiber hybrid piezo-triboelectric nanogenerator with a power density of 0.31 mW/cm². Sun *et al.* [33] presented a piezo-triboelectric energy harvester with a maximum voltage of 150 V under high-temperature stability of 200℃.

Flexible piezoelectric materials have also attracted considerable

attention due to their stretchability in adhesive quality to the human body [34–36]. Zhou *et al.* [37] proposed a study that utilized 3D printing technology to print flexible piezoelectric converters with a maximum power density of 1.4 μW/cm^2 at the resistance of 10^7 Ω. Zhang *et al.* [37] developed a stretchable piezoelectric nanogenerator that replaced silver electrodes with graphene-assembled macro-film. Ji *et al.* [38] presented a wearable generator based on core–shell piezoelectric yarn. The maximum output power value is around 0.97 μW by body bending movements. Waseem *et al.* [39] proposed PEHs based on a 6 mm thick Al$_2$O$_3$ shell with a current density of 100nA/cm^2. Wang *et al.* [40] fabricated PEHs with an energy conversion efficiency of 0.02%. Mokhtari *et al.* [41] demonstrated a nanofibers-based PEH which generated a voltage of 3 V at the frequency of 200 Hz. Zhong *et al.* [42] developed a new type of flexible PEH with a peak power of 0.444 mW under the pressure of a human hand. Mark Meschino *et al.* [43] developed flexible PEHs in constant thickness design that generated maximum power of 4.1623 μW. A novel stretchable PEH proposed by Kim *et al.* [44] could be directly attached to garments by the hot-press approach. Han *et al.* [45] demonstrated a micro piezoelectric sensor with a short-circuit current of 497.3nA. The sensor can monitor the state of human motion. Stretchable epidermal devices can adapt to flexible deformations of the human body with sizeable mechanical compliance for human health monitoring.

Traditional piezoelectric materials display high impedance and low capacitance (nano-level), which collectively result in low power output. Recent studies proved the advantages of piezoelectric stacks (PES) over conventional piezoelectric materials[46–49]. The capacitance of PES is much larger than that of a single piezo patch of the same volume, which reduces the increase of dynamic resistance, rustling higher power response. Therefore, increasing attention is getting drawn to energy harvesting via PES. Wang *et al.* [50] designed a PEH based on PES for pavements, which reached a maximum output power of 11.67 mW with the optimum load of 10 kΩ under a pressure of 0.7 MPa and 15 Hz. Khalili *et al.* [51] developed a vehicle movement mechanical energy generator based on PES. The generator could generate a square power of 9 mW for an external resistor of 50 kΩ under excitation of 66 Hz. Chen *et al.* [52] presented a two-stage PES energy generator. The prototype achieved a power density of 487 mW/g^2 at resonance. Although the output power of the above studies has been significantly improved, they are based on medium- or high-frequency vibration excitation. Few literatures have been found targeting at scavenging ultra-low frequency vibration energy with PES regardless of its extensive existence especially exemplified by human motions.

Human motion is mostly ultra-low frequency (≤5 Hz) vibration, which causes harvesters a low energy conversion efficiency and low-power output. Therefore, achieving real-time sensing with self-powering has been challenging by capturing vibration energy from human motion based on PES.

This study proposes a piezostack-based frequency-converted generator emphasizing ultra-low frequency vibration energy harvesting to achieve real-time self-powered wearable sensors with ample redundant charges. Key novelties and contributions are: first, a significant decrease of the matched impedance of PEH. The stack consists of 180 units, which dramatically increases the capacitance of the material, decreasing the dynamic resistance of PES. Second, a force amplifier to magnify the compressive force and to improve the output voltage and power of the generator. Third, through the spring-mass system and the collision between the proof mass and spring limiter, the ultra-low frequency human motion is converted into high-frequency vibration, which again effectively reduces the matching impedance of the generator. As such, the instantaneous peak-to-peak output power is 5.56 W at a running speed of 10 km/h. Finally, demonstration of desirable output performance to sustain power requirement of wearable sensing with substantial quantity of redundant charges exemplified by a watch and a thermometer.

2. Structural configuration and governing equations

2.1. Structural design

The PES can generate a great number of charges by enduring high external excitation resulting in large acceleration or force in compression mode in short-circuit condition. In human running motions, each step can be seen as a pulse with an acceleration of 2 g approximately. By a spring limiter, the amplitude of proof mass is truncated. The amplitude truncation induces a nonlinear behavior [53–57]. So that an over 100 N impact force is applied at the piezo-stack. Accordingly, it satisfies the excitation request of the PES-based harvesters in the running for high performance.

The proposed structure configuration, displayed in Fig. 1(a), consists of four main components: a force amplifier, a PES, a spring-mass system, and a spring limiter. The spring-mass system is connected to the force amplifier via the rod. The PES is secured in the amplifier. The whole structure is fixed to a mounting frame by the amplifier.

Multiple piezoelectric units constitute the PES. Each unit is made of multiple piezoelectric ceramic and silver layers placed between ceramic layers as electrodes. When the PES is stressed by force (*F*) in the polarization direction, the voltage of the PES (*U*) is calculated as follows:

$$U = \frac{g_{33}dF}{A} \tag{1}$$

in which g_{33}, d, and A are the piezoelectric constant, thickness of the PES, and stressed area of the PES, respectively.

While exposed to external excitation, the generator responds with the reciprocating motion of the mass. When the amplitude of the mass is greater than the initial distance between the limiter and the mass, impacts occur, resulting in large impact force (up to hundreds of newtons). The forces are further transmitted to the stack (Fig. 1(b)), inducing electric potential between electrodes of each piezo layer. Fig. 1(c) demonstrates the force transmission along with the force amplifier. We denote that F_1, F_2, and α are the external excitation force, the force along the connecting rod, and the angle between the connecting rod and PES, respectively. At junction A, we can calculate F_1 as follows:

$$F_1 = 2F_2 sin\alpha \tag{2}$$

Similarly, at junction B,

$$F = 2F_2 cos\alpha \tag{3}$$

The force amplification ratio can be calculated via integrating Eqs. (2) and (3).

$$\frac{F}{F_1} = \frac{1}{tan\alpha} \tag{4}$$

As larger *F* results in higher voltage according to Eq. (1), choosing a small angle α is recommended.

2.2. Theoretical analysis and hypothesis

In the process of harvesting energy from human motions, the motion of the proof mass concerning the amplifier and the limiter produces an impact, inducing a micro-elastic deformation of the force amplification mechanism. The force amplifier, the spring limiter, and the rod can be regarded as another equivalent spring-mass system and serve as another degree of freedom (DOF) in the generator. The equivalent spring-mass system converts the ultra-low frequency excitation into a high-frequency oscillation response. Fig. 1(d) demonstrates an equivalent model of the system. The proof mass is presented as m_1. The equivalent mass m_2 contains the rod, spring limiter, force amplifier, and piezo stack. We use k_i and c_i ($i = 1, 2$) to denote the equivalent spring stiffnesses and damping coefficients, respectively. The 2DOF energy capturing system can be defined by the electro-mechanical coupling governing equations:
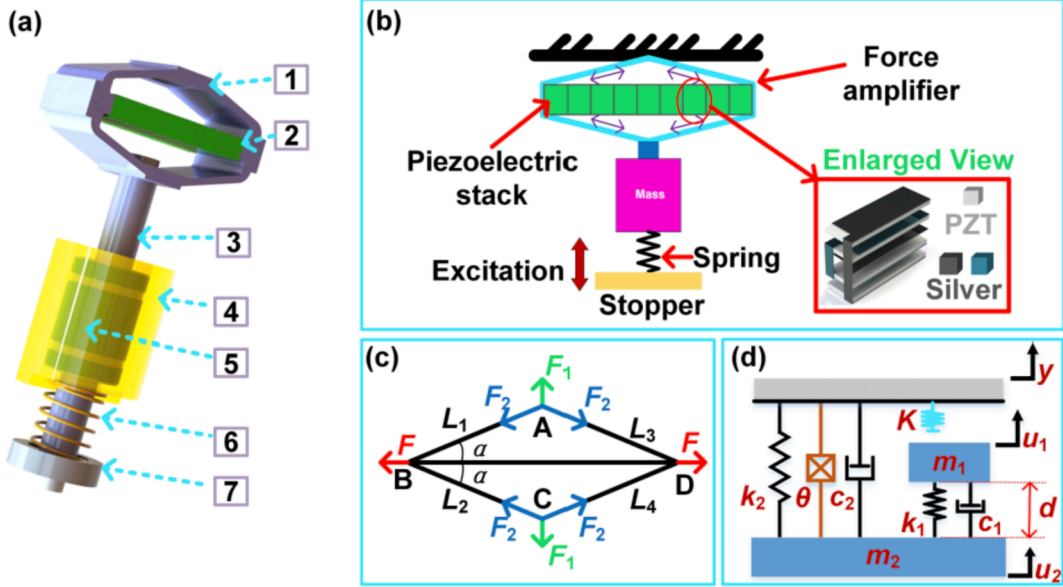
Fig. 1. Design and schematic of the generator: (a) the structural configuration of the generator. The crucial components are: 1. force amplifier 2. piezoelectric stack 3. rod 4. proof mass 5. sliding bearing 6. spring 7. spring limiter. (b) schematic of the generator and unit structure of the PES. (c) force analysis along with the force amplifier. (d) the schematic of the 2DOF model.

$$\begin{cases} -m_1\ddot{y} = m_1\ddot{u}_1 + c_1(\dot{u}_1 - \dot{u}_2) + k_1(u_1 - u_2) + p(u_1, u_2) \\ -m_2\ddot{y} = m_2\ddot{u}_2 + c_2\dot{u}_2 + k_2u_2 + c_1(\dot{u}_2 - \dot{u}_1) + k_1(u_2 - u_1) - p(u_1, u_2) + \theta v \\ \theta\dot{u}_2 = \dfrac{v}{R} + C_p\dot{v} \end{cases}$$

(5)

in which u_i ($i = 1$, 2), y, v, R, C_p, and θ are the displacements of the equivalent mass m_1 and m_2 in relation to the frame, the displacement of the frame, the open-circuit voltage of the generator, the load resistance, the capacitance of the PES, and the electro-mechanical coupling coefficient, respectively. The dot notations on the parameters (u_i, y, and v) represent the derivative of time.

When the generator is at the initial position, the motion of the mass induces the compression of the spring. We denote d as the distance of the m_1 and m_2 in the initial state. When the relative distance between m_1 and m_2 is smaller than d, i.e., without the impact, the deformation of the spring constitutes the force applied onto the force amplifier. Therefore, the impact force $p(u_1, u_2)$, which can be considered as linear one [58,59], is described by the equation:

$$p(u_1, u_2) = \begin{cases} K(u_1 - u_2 + d) & u_1 - u_2 < -d \\ 0 & u_1 - u_2 \geqslant -d \end{cases}$$

(6)

We denote K as the collision stiffness of the limiter in the equivalent spring-mass system during the impact.

By defining the following parameters: $x_1 = u_1, x_2 = \dot{u}_1, x_3 = u_2, x_4 = \dot{u}_2, x_5 = v$; the state-space representation of governing equations can be rearranged as follows:

$$\begin{cases} \dot{x}_1 = x_2 \\ \dot{x}_2 = -\ddot{y} - \dfrac{1}{m_1}[c_1(x_2 - x_4) + k_1(x_1 - x_3) + p(x_1, x_3)] \\ \dot{x}_3 = x_4 \\ \dot{x}_4 = -\ddot{y} - \dfrac{1}{m_2}[c_2x_4 + k_2x_3 + c_1(x_4 - x_2) + k_1(x_3 - x_1) - p(x_1, x_3) + \theta x_5] \\ \dot{x}_5 = \dfrac{1}{C_p}\left(\theta x_4 - \dfrac{x_5}{R}\right) \end{cases}$$

(7)

$$p(x_1, x_2) = \begin{cases} K(x_1 - x_3 + d) & x_1 - x_3 < -d \\ 0 & x_1 - x_3 \geqslant -d \end{cases}$$

(8)

The primary goal of this study is to collect and convert the kinetic energy of human running motion. Thus, to mimic such motions, we set the base excitation frequency and displacement amplitude at 2.5 Hz and 0.1 m, respectively. Fig. 2(a) depicts the voltage response of the governing equations solved numerically in MATLAB. A detailed demonstration in Fig. 2(b) shows the voltage responses coupling high-frequency (~2000 Hz) oscillation and the rest of the low-frequency harmonic response. Each response is composed of three high-frequency oscillations. In each cycle, the duty ratio from the generator is around 37.5%. Also, the oscillation peak-to-peak voltage reaches as high as 19.5 V, contributing majorly to the total power generation.

As the frequency and amplitude of human running motion can vary with time, we then simulated the cases with the excitation frequency varying from 2 Hz to 3 Hz and the displacement from 0.06 m to 0.14 m, respectively. The voltage responses (Fig. 2(c)) under 2 Hz and 3 Hz are almost the same pattern as that of the 2.5 Hz case. The results in the frequency and excitation amplitude domains, illustrated in Fig. 2(d) and (e), respectively, indicate that the voltages increase as the frequency and excitation amplitude increase. This trend is relatively evident as the excitation grows more and more intense. Note that the oscillation frequency decides the dynamic resistance of the stack, and high frequency can significantly enhance the output current. Therefore, we hypothetically anticipate high power output that can satisfy the power requirement of low-power wearable sensors and electronics.
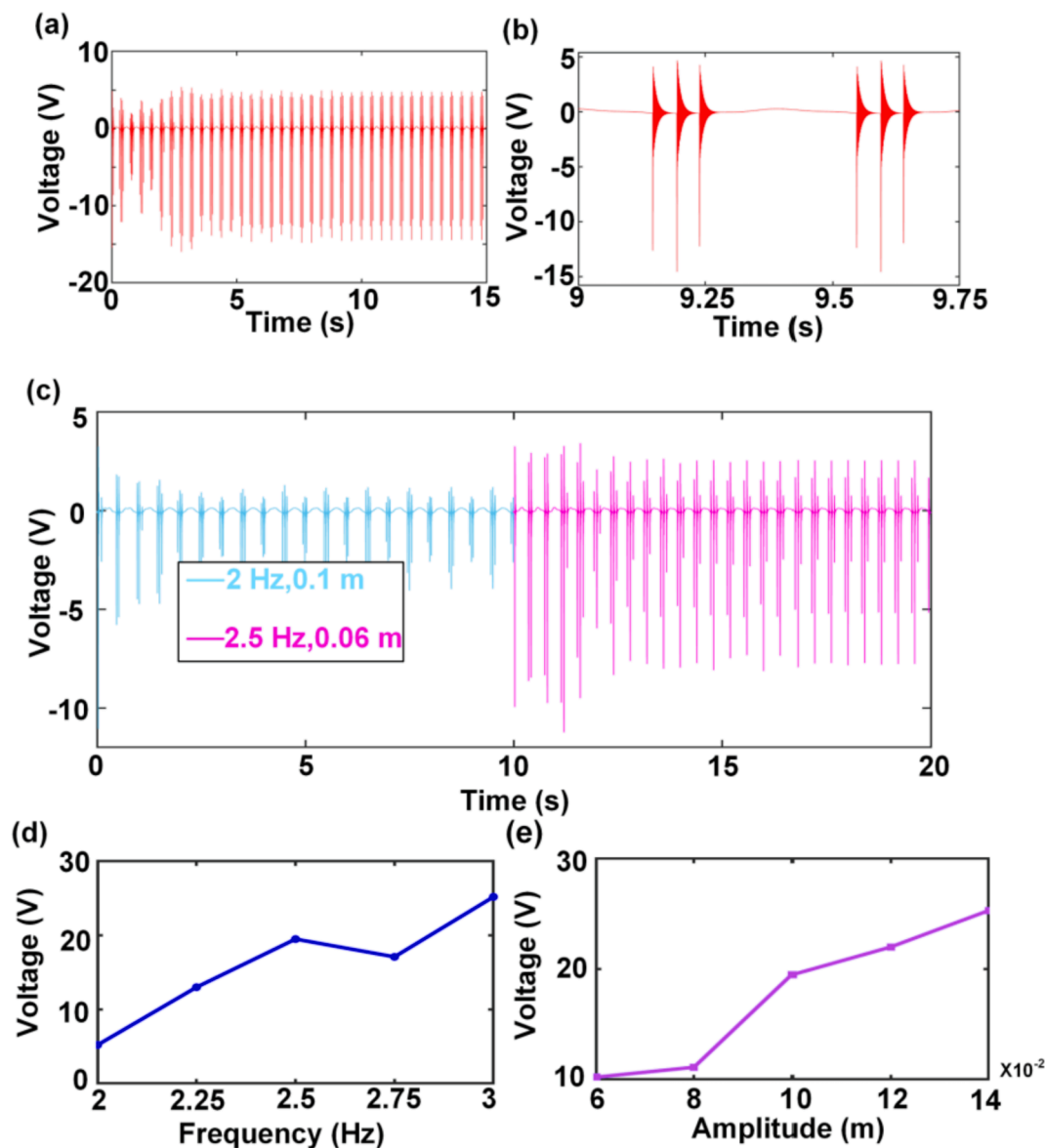
Fig. 2. Numerical results: (a)&(b) voltage response and detail (9 to 9.75 s) under the base excitation frequency and displacement amplitude at 2.5 Hz and 0.1 m, respectively. (c) voltage responses under different excitation conditions (2 Hz and 0.1 m; 2.5 Hz and 0.06 m). (d) voltage responses under different base excitation frequencies (2 Hz to 3 Hz). (e) voltage responses under different displacement amplitudes (0.06 m to 0.14 m).

3. Experimental validation and discussion

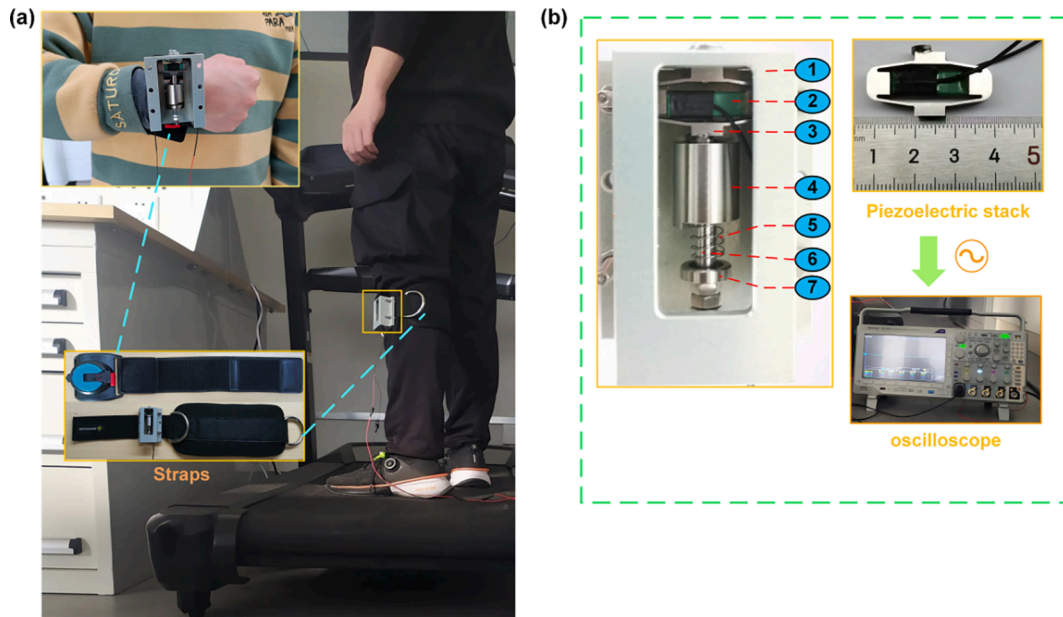### 3.1. Experiment setup and prototype fabrication

A prototype (the prototyping illustrated in Fig. 1(a)) was fabricated. Afterward, we conducted experiments to examine the output characters and validate the theoretical analysis. Fig. 3 displays the overall experiment setup. In running experiments, the excitation on the prototype is imposed from a male (25 years old, 80 kg, ~1.75 m) running on a treadmill (Nautilus T686). The prototype was strapped slightly (~3 cm) below the knee of the subject (shown in Fig. 3(a)) by a leg strap (Manuekleak ML103). We selected this position for two reasons: during running, the motion amplitude of the shank is greater than that of the thigh. The shank shape is a spindle-like shape that is wide in the middle, and the prototype does not fall off the shank easily. The device was placed vertically when the subject stood straight. Then, we used a wrist strap (OOPSCOOL XW-X01) to attach the harvester to the wrist of the subject in the hand-waving experiments. The rod of the prototype is always perpendicular to the arm.

All the parts were attached to the mounting frame. All output electrical signals, such as peak-peak voltages and currents, were measured and recorded from an oscilloscope. The metal parts of the prototype, except the spring (spring steel) and the mounting frame (aluminum 7075), were made of stainless steel. The primary materials of the straps are stainless steel and ethylene–vinyl acetate copolymer (EVA). Detailed material properties and geometry dimensions of the prototype are listed and illustrated in Table 1.

3.2. Open-circuit voltage response and frequency conversion

We firstly examined the open-circuit voltage which is shown in Fig. 4 (a) and (b), under different speeds of the treadmill (4 km/h, 6 km/h, 8 km/h, 10 km/h, 12 km/h) and different spring stiffnesses (0.05 N/mm, 0.29 N/mm, 0.49 N/mm, 0.98 N/mm, 2 N/mm). For the experiments with different speeds, we singled out the spring of 0.49 N/mm stiffness for the experiments. For the different spring stiffnesses, we chose the 10 km/h speed for the experiments.

In Fig. 4(a) and (b), the motion speed plays a vital role in the

Fig. 3. Experiment setup and prototype fabrication. (a) Installation setup of the prototype. (b) The main components of the 2DOF PEH include: 1. mounting frame 2. PES 3. force amplifier 4. proof mass 5. spring 6. rod 7. spring limiter.

Table 1
Detailed dimensions and material properties.

Description		Value
PES	Piezoelectric material	PZT-5H
	Number of layers	180
	Young's modulus (GPa)	62
	Piezoelectric constant g_{33} (10^{-3} V m/N)	12.5
	Capacitance (μF)	1.986
	Density (kg/m^3)	8000
	Dimension (mm^3)	$5 \times 5 \times 18$
Force amplifier	Intersection angle: α (rad)	0.3
	Dimension (mm^3)	$12 \times 15 \times 28.9$
	Thickness (mm)	0.5
Proof mass	Mass (g)	22.45
Spring	Stiffness (N/mm)	0.05,0.098,0.29,0.49,0.98,2
	External diameter (mm)	8
	Free length (mm)	10
PEH	Dimension (mm^3)	$16 \times 29.1 \times 65.5$

resultant voltage. The peak-peak voltage increases with the increasing speeds. With the spring stiffness of 0.49 N/mm, as the speed changes from 4 km/h to 6 km/h, the peak-to-peak voltage varies from 2.59 V to 15.49 V. The reason for such a distinct voltage growth is that at the speed of 6 km/h, the motion of the subject switched from walking to running, leading to an evident increase of the motion amplitude of the shank. Then, as the speed further increases, the collision between the mass and the limiter becomes more intense and frequent. The peak-peak output voltage increases and reaches as high as 24.82 V.

The spring stiffness also demonstrates a decisive influence on the peak of the voltage pulses. For the experiments with 10 km/h speed and different spring stiffnesses, with the spring stiffness of 0.05 N/mm, the maximum value of peak-peak voltage is 24.44 V. With the increase of the stiffness from 0.29 N/mm to 2 N/mm, the peak-peak voltage decreases from 20.56 V to 11.81 V (Fig. 4(b)). The spring acts as a buffer between the mass and the limiter. As the stiffness increases, the potential energy stored by the spring is increased. As such, the decrease of the kinetic energy of the mass leads to lower impact force and, thereby, lower force applied on the force amplifier. According to Eq. (1), the force is proportional to the voltage, so the rise of the spring stiffness constitutes the reduction of the maximum peak-peak voltage.

Subsequently, we conducted hand-waving experiments at about 3.5 Hz, and the time-history voltage output is depicted in Fig. 4(c). The resulting peak-to-peak voltage amplitude is 9.14 V. The conversion frequency is around 2082 Hz, displayed in the detailed voltage pulse. The excitation force in the hand-waving experiments is weaker than that in the running experiments. According to Eq. (1), the voltage generated by the piezoelectric stack decreases with the weakening force. Thus, the voltage amplitude declines markedly despite increasing excitation frequency.

Given the spring stiffness of 0.05 N/mm and the treadmill speed of 10 km/h (which is approximately 2.5 Hz), comparing the detailed voltage pulses from the experiment and the simulation (the excitation frequency and displacement amplitude are at 2.5 Hz and 0.1 m, respectively) is shown in Fig. 4(d). The frequency of the voltage response in the time domain, both simulated and experimental, is about 2000 Hz. The peak-to-peak amplitude of the experimental results is 18.08 V, in good agreement with that of the analytical results that is 19.24 V. The value of the experimental result is opposite to that of the simulation result because the polarity of the oscilloscope probe in the experiment is opposite to that of the prototype electrode.

The experiment and simulation frequencies of instantaneous voltage responses under different spring stiffnesses are demonstrated in Fig. 4 (e). With the increase of the spring stiffness from 0.05 N/mm to 2 N/mm, the peak-peak voltage decreases from 24.44 V to 11.81 V indicated in Fig. 4 (b), which means lower impact forces on the force amplifier. A distinct trend that the frequency up-conversion effect fades as the decline of the forces is depicted in Fig. 4 (e). Predictably, as the spring stiffness increases beyond a threshold, the impact will be weakened further, and the frequency up-conversion effect will be difficult to occur or scarcely occur. The simulation results are in excellent agreement with the experiment results. The piezo stack is dielectric when no external force or vibration is imposed [60,61]. The dynamic impedance, i.e., the impedance under vibration, is determined by the high-frequency oscillation instead of the running motions. The following section will elaborate and discuss this influence of frequency up-conversion on the PES inner electric impedance.

3.3. Matched impedance and power output

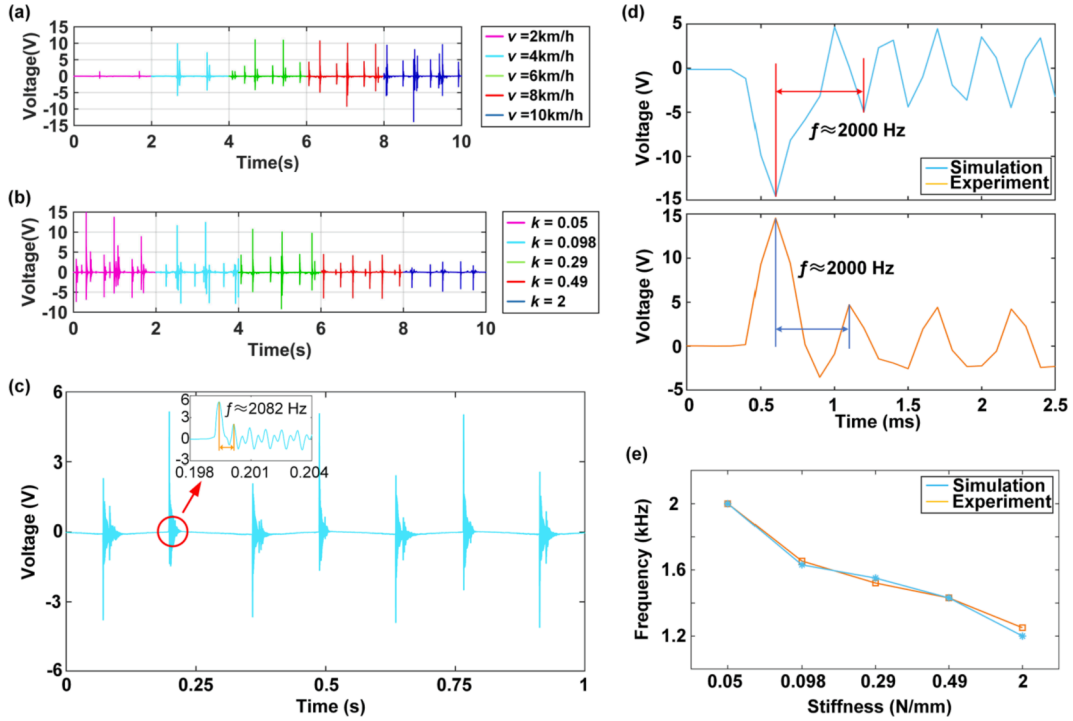To examine the output performance of the generator further, we

Fig. 4. Open-circuit voltage responses under different experiment conditions: (a) instantaneous peak-peak voltage under spring stiffness of 0.49 N/mm and different speeds ranging from 4 km/h to 12 km/h. (b) instantaneous peak-peak voltage under the speed of 10 km/h and different spring stiffnesses of 0.05–2 N/mm. (c) the instantaneous voltage output from the hand-waving experiment. (d) comparison of the time-domain voltage output results from the experiment and the simulation. (e) the experiment and simulation frequencies of instantaneous voltage responses from different spring stiffnesses ranging from 0.05 N/mm to 2 N/mm.

recorded the terminal voltage of different resistors. The experimental conditions were set as follows: the spring stiffness was 0.05 N/mm; the treadmill speed was 10 km/h. The equation of the theoretical matched impedance of the generator is[62]:

$$R_m = \frac{1}{2\pi f C_p} \tag{9}$$

in which f is the frequency of high-frequency oscillation. With the capacitance (1.986 μF) from Table I and the frequency (2000 Hz) mentioned above, we obtain the estimated optimal external resistance as 40 Ω.

Fig. 5(a) and (b) display the instantaneous power & voltage and the current, respectively. The output voltage rises to 29.53 V with the increasing external load. It is close to the voltage under the open-circuit

condition. Then we obtain the instantaneous power (P_{p-p}) via the equation below:

$$P_{p-p} = \frac{\left(V_{p-p}\right)^2}{R} \tag{10}$$

where V_{P-P} and R represent the peak-peak voltage and external load, respectively.

With the growth of the load, the peak-peak power increases and reaches the maximum, 5.56 W, under the resistance of 39.6 Ω. It is in excellent agreement with our estimation. After that, the output power decreases to a trivial microwatt level with the increasing value of the external resistors. Fig. 5(c) demonstrates the current responses under resistances ranging from 5 Ω to 100 Ω. Meanwhile, the current declines to a trivial microampere level with the rise of the load. Fig. 5(d) portrays
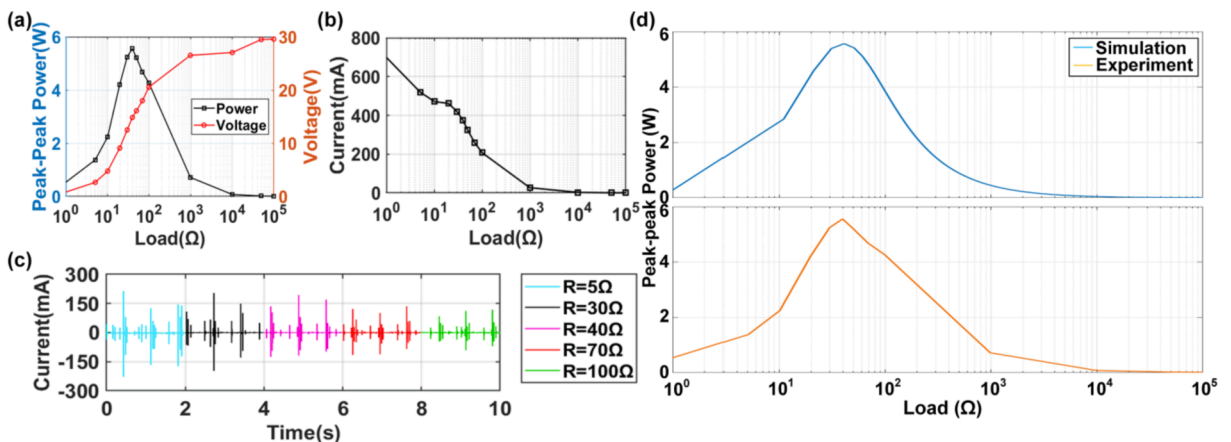

Fig. 5. Output voltage & power and current of the generator: (a) peak-peak voltage and instantaneous power. (b) current. (c) current responses with different resistances. (d) comparison of the load-domain power results from the experiment and the simulation.

the load-domain power results from the experiment and the simulation (the theoretical acquisition of output power is listed in Appendix A) for comparison. The matched impedance and peak power of the simulation are 41 Ω and 5.575 W, respectively. The trend and value of the analytical results are in excellent agreement with the experimental results.

As illustrated in Fig. 4(d) and (e), the frequency of the high-frequency oscillation is 2000 Hz. According to Eq. (9), the dynamic resistance is inversely proportional to the oscillation frequency. A significant increase in the oscillation frequency will dramatically decrease the matched impedance. Moreover, voltage amplitude depends only on the external excitation. Since the instantaneous power is inversely proportional to resistance, the decrease of dynamic resistance induces a considerable increase in output power.

Then, the maximum average power is calculated as 0.92 mW by the equation.

$$P_{avg} = \int_0^T \frac{U^2(t)}{R_m} dt \tag{11}$$

in which $U(t)$, R_m, P_{avg}, and T are instantaneous voltage, matched impedance, average power, and the excitation duration, respectively. In an excitation cycle, the dynamic behavior of the harvester falls into a high-frequency oscillation and low-frequency vibration. The peak-to-peak voltage amplitude of high-frequency oscillation is tens of times than that of low frequency. However, the duration is the opposite. The duty ratio of the prototype is usually around 40%. Therefore, the average power is much less than instantaneous power.

Stretchable epidermal devices can better attach to the human body because of elastic extension. However, due to low piezoelectricity, the average power and peak power of stretchable piezoelectric energy harvesters is μW level [38–43] and mW level [42] while most matched impedances range from hundreds of kΩ even to dozens of MΩ [37]. The proposed generator can reach the uttermost power of 5.56 W with the matching impedance of 39.6 Ω. The maximum average power is 0.92 mW under the excitation frequency of around 2.5 Hz. Compared with stretchable epidermal devices, the proposed generator achieves higher output power at small matched impedance.

Table 2 depicts an output performance comparison for the proposed 2DOF PEH and other harvesters with the frequency up-conversion mechanism. The matching impedance of the 2DOF PEH is less than those of others, and the average power is greater at a comparatively weaker excitation condition from Table 2.

3.4. Experiments of powering LEDs

In Section 3.3, the generator generated the maximum instantaneous power of 5.56 W, which displays excellent potential for powering electronics and sensors. To further test the charging capacity of the generator, a series of experiments were carried out. Fig. 6(a) represents the experimental circuit. We chose different appliances controlled by switches. Firstly, we conducted the lighting experiment (the switches S1 and S2 on, the others off). The excitation was the same as that in Section 3.3. The working voltage of the LEDs, which is the red color when lit up, is 1.67 V. A 'SHU' (short for Shanghai University) array consisting of 46 diodes lighted up successfully. Fig. 6(b) displays the lighted LED array.

To depict the blinking process of LED array precisely, we recorded the terminal voltage of the LEDs (Fig. 6 (c)). The array was lighted up with the terminal voltage exceeding the working voltage (1.67 V). The LED array can be regarded as a capacitor that can store redundant charges when extinguished. Hence, the terminal voltage is sustained at around 1 V. We have demonstrated that the response voltage frequency of the generator is considerably higher than the excitation frequency due to the frequency up-conversion effect in the previous section. In a single excitation, the LED array is lighted up with the voltage exceeding the operating voltage; when the voltage falls below the threshold, the LED goes out, and the generator continues to charge the capacitor. When the capacitor voltage reaches the LED operating voltage, the LED array lights up. Thus, the blinking frequency is greater than that of the running motions.

3.5. Experiments of charging capacitors

In the capacitor-charging experiments, we investigated the saturation voltage and average charging power of different capacitors charged by the generator. The excitation conditions were set the same as in Section 3.4 (switches S1 and S2 on, the others off in Fig. 6(a)). In the experiments, we employed four different capacitors: 220 μF, 470 μF, 1000 μF, and 3300 μF.

Fig. 7(a) illustrates the terminal voltages of the different capacitors in the running experiments. The termination voltages vary with the different capacitances. With the increase of the capacitance, the maximum voltage decreases. We set the charging time to 120 s. The final voltage of the 220 μF capacitor is 11.01 V. The saturation voltage of the 470 μF capacitor is 9.89 V, slightly lower than that of the 220 μF capacitor. Then, the saturated voltages of 1000 μF and 3300 μF capacitors are 5.83 V and 2.59 V, respectively. We then conducted capacitor charging tests for handwaving. The charging time is 20 s. The final charging voltages of the cases with capacitances of 470 μF, 1000 μF, and 3300 μF are 2.274 V, 1.415 V, and 0.767 V, respectively. The case with the capacitance tuned to 220 μF yields the maximum charging voltage, i. e., 2.95 V.

The average charging power (P_a) is.

$$P_a = \frac{C_p(U_2^2 - U_1^2)}{2t} \tag{12}$$

in which C_P, U_1, U_2, and t represent the capacitance, initiation voltage, termination voltage, and charging time, respectively.

Fig. 7(c) displays the average power of charging different capacitors. For example, the maximum charging power for the 470 μF capacitor is 192 μW and 61 μW from the running and hand-waving experiments, respectively. Fig. 7(c) clearly illustrates the average charging power gap between the running and hand-waving experiments. Although the up-conversion frequency is elevated in the hand-waving experiments, the excitation is considerably weaker than that in the running experiment. Hence, charges elicited from the piezoelectric stack are significantly fewer, resulting in far less charging power than in the running experiment.

Table 2
Summary of frequency up-conversion energy harvesters.

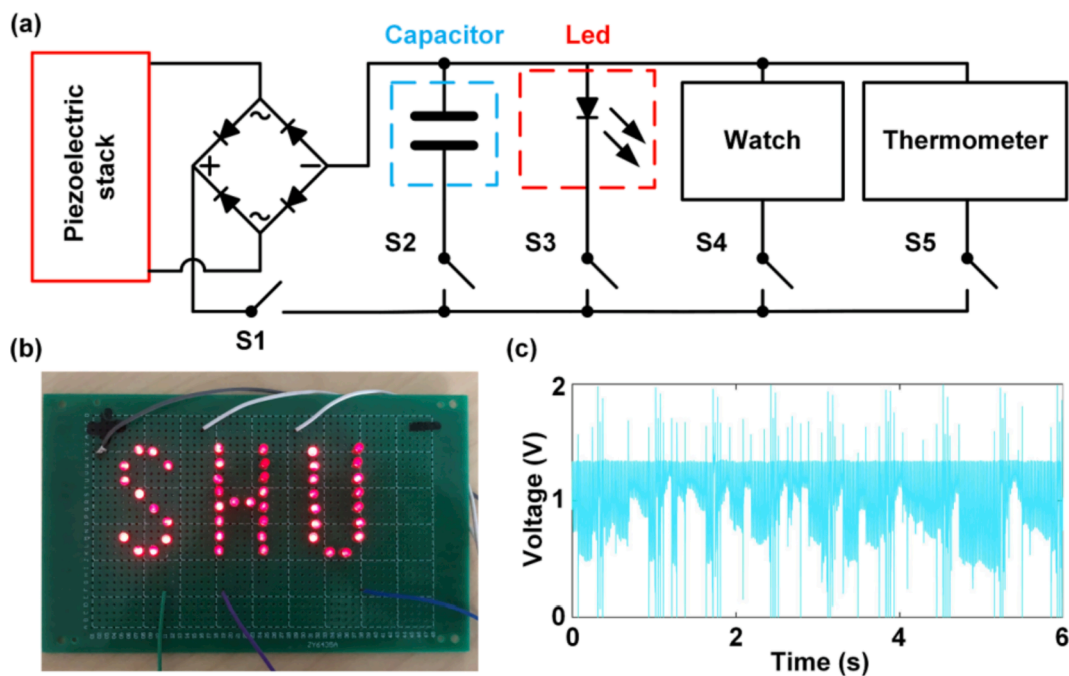| Refs.	Dimensions (mm³)	Mechanism	Matching Impedance (kΩ)	Excitation	Average Power (mW)
[8]	Ø14 × 42	Electromagnetic	0.05	15 Hz, 20 ms^{-2}	0.96
[13]	40 × 25 × 58	Hybrid	0.192	12.5 km/h	75
[27]	17.35 × 40 × 90	Hybrid	1.15 k	4 Hz	0.006
[58]	Ø70 × 8	Piezoelectric	16	24 Hz, 1 g	0.75
[63]	Ø70 × 15	Piezoelectric	15	2.5 km/h	0.52
This paper	16 × 29.1 × 65.5	Piezoelectric	0.0396	10 km/h	0.92

Fig. 6. The circuit and powering LEDs: (a) the circuit for powering electronics. (b) the lighted LEDs array. (c) the terminal voltage of the LEDs array. The lighted LEDs are demonstrated in a video in the supplementary files.
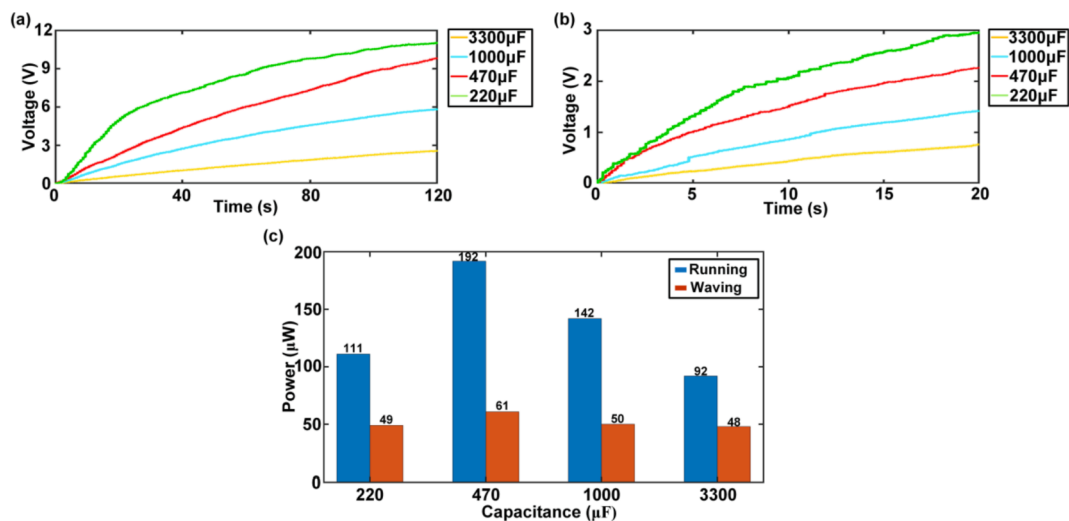

Fig. 7. Charging performance of the PEH: (a) charging curves in the running experiments; (b) charging curvatures in the hand-waving experiments; (c) the average charging power of the running and hand-waving experiments.

3.6. Self-powered applications with ample redundant charges

Then, we further examined the application performance of the generator to build a self-powered electronic watch (C-SPORT 0119, 3 V nominal voltage), and the minimum voltage required by this watch is slightly above 2 V. In the circuit of Fig. 6(a) (switches S1, S2, and S4 on, the others off), we first removed the coin battery and connected the watch, rectifier, and capacitor (2.2 mF, 25 V) in parallel and then charged the watch for 150 s at a speed of 10 km/h and with 0.05 N/mm spring stiffness. The real-time terminal voltage is displayed in Fig. 8(a).

In stage I, the voltage rises to 2.1 V in 52 s, at which the watch begins to tell time. In stage II, charges continue getting accumulated into the capacitor, and the voltage continues increasing to 4.484 V as the subject keeps running. A large number of redundant charges generated by the generator are stored in the capacitor, which is regarded as a battery

when the subject stops running. The phenomenon demonstrates that the generator is sufficient to realize the real-time self-powering of the watch.

In stage III, after the running motion of the subject is suspended, the capacitor continues to serve as a battery for the watch. As the watch is working, the voltage decreases and eventually drops to 2.008 V, at which level the watch becomes challenging to display time, and the watch stops working. Compared with the 150 s charging time of the first two stages, the redundant charges are still able to power the watch for approximately 50 minutes.

Afterward, we examined the performance of charging a thermometer (MITIR 6811623, 3 V nominal voltage). In the circuit displayed in Fig. 6 (a) (switches S1, S2, and S5 on, the others off), a capacitor (2.2 mF, 25 V) was connected in parallel with the thermometer, whose battery was removed. The excitation was set the same as that of the experiment of charging the electronic watch. To depict the operation process of the
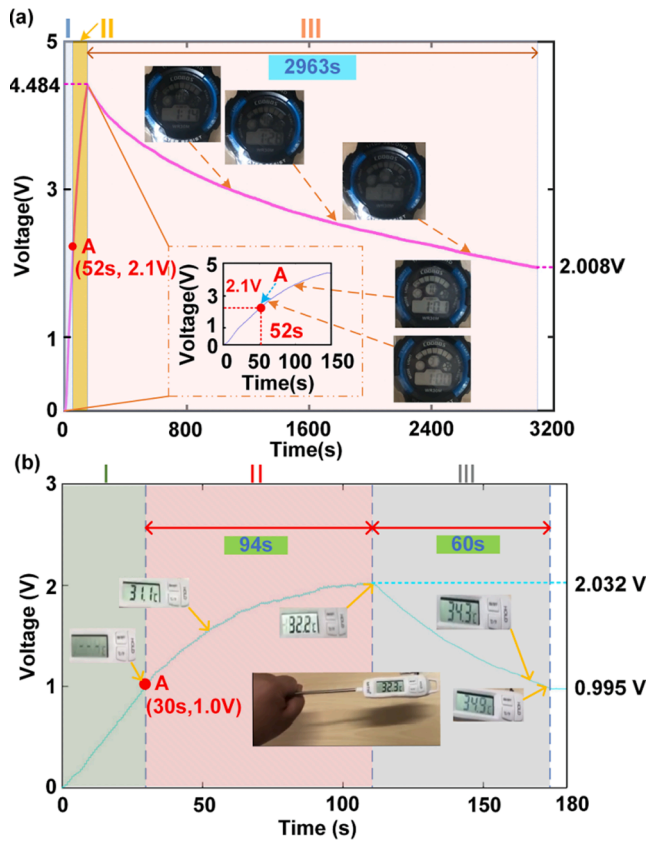
Fig. 8. Terminal voltages of the watch and the thermometer in real-time. (a) terminal voltages of the watch. (b) terminal voltages of the thermometer. The real-time powering is illustrated in videos in the support files. Stage I, II, and III are the charging stage, charging & real-time powering stage, and discharging stage.

thermometer in detail, we recorded the terminal voltage of the capacitor displayed in Fig. 8(b), which was regarded as a power source.

In the first 30 s, the terminal voltage reaches 1.0 V. At the same time, the LED screen is lighted up, and the thermometer starts to measure the temperature of the subject's palm. In stage II, the generator continued to charge the capacitor for 94 s, and the voltage further to 2.032 V.

To validate the functionality of the thermometer, we measured the temperature of the subject's palm throughout three stages, of which the actual value further verified the result.

In stage III after the excitation stops, the thermometer continues to operate for about 60 s. It is redundant charges in the capacitor that continues powering it. The results demonstrate that the generator can power the sensor in real-time and simultaneously store extra charges into the capacitor. The voltage drops to 0.995 V while the LED screen is off and the thermometer stops working.

The watch and thermometer functioned properly without excitation in the experiments, relying on substantial redundant charges. Predictably, with the continuation of the subject's running, the generator can completely replace the battery of the watch or the thermometer as a continuous power supply. The experimental results prove that the output performance of the generator is sufficient to realize real-time self-powered sensing.

4. Conclusion

In this paper, we proposed a piezostack-based frequency-converted generator that absorbs vibration-based energy in human ultra-low frequency motions to achieve real-time self-powered sensing for wearables. The generator consists of a piezoelectric stack, a force amplifier, a spring-mass system, and a spring limiter. The impact force induced by amplitude truncations of the spring-mass system causes the frequency up-conversion effect. A 2DOF model was built to estimate the responses of the generator and examine the frequency up-conversion effect. Then, we fabricated a prototype and conducted five series of experiments to examine the output performance and draw conclusions as follows:.

1) The numerically estimated voltage responses depicted the high-frequency oscillation in each cycle and resulted in a peak-peak open-circuit voltage over 20 V. Moreover, the generator voltage increases with the rise of excitation amplitude and frequency.
2) The frequency up-conversion effect is further validated by experimental studies contributing to dramatically lowered matched impedance (39.6 Ω) and much higher instantaneous peak power output at the running speed of 10 km/h.
3) The generator proves capable of real-time powering low-power sensors and generating ample redundant charges to continue powering after the excitation is suspended. With the 150 s charging time, the extra stored charges can power a watch to keep working for approximately 50 minutes, around 20 times as long as the charging phase.

The generator demonstrates great potential to harvest ultra-low frequency vibrations with instantaneous power reaching Watt level. The realization of powering wearable sensors with ample redundant charges based on a millimeter-sized generator provides a novel angle for developing high-performance self-powered sensing from the kinetic energy of human motions. As the response and outputs are closely related to structural parameters, future work can be emphasized on systemic distributed model formulation, analytical solution, and optimization for the best performance.

CRediT authorship contribution statement

Zhongjie Li: Conceptualization, Writing – review & editing, Methodology, Resources. **Xuzhang Peng:** Writing – original draft, Investigation, Formal analysis. **Guobiao Hu:** Software, Formal analysis. **Dong Zhang:** Writing – original draft. **Zhibing Xu:** Writing – original draft, Investigation. **Yan Peng:** Supervision, Project administration, Funding acquisition. **Shaorong Xie:** Funding acquisition, Supervision.

Declaration of Competing Interest

The authors declare that they have no known competing financial interests or personal relationships that could have appeared to influence the work reported in this paper.

Acknowledgments

Appendix A. Supplementary data

Supplementary data to this article can be found online at https://doi.org/10.1016/j.enconman.2022.115466.

References

[1] Li Z, Liu Y, Yin P, Peng Y, Luo J, Xie S, et al. Constituting abrupt magnetic flux density change for power density improvement in electromagnetic energy harvesting. Int J Mech Sci 2021;198:106363.
[2] Lu Z-Q, Wu D, Ding H, Chen L-Q. Vibration isolation and energy harvesting integrated in a Stewart platform with high static and low dynamic stiffness. Appl Math Model 2021;89:249–67.

[3] Z. Li, C. Xin, Y. Peng, M. Wang, J. Luo, S. Xie, et al. Power Density Improvement of Piezoelectric Energy Harvesters via a Novel Hybridization Scheme with Electromagnetic Transduction. 12 (2021) 803.

[4] Peng Y, Zhang D, Luo J, Xie S, Pu H, Li Z. Power density improvement based on investigation of initial relative position in an electromagnetic energy harvester with self-powered applications. Smart Mater Struct 2021;30(6):065005.

[5] Lu Z-Q, Zhao L, Ding Hu, Chen L-Q. A dual-functional metamaterial for integrated vibration isolation and energy harvesting. J Sound Vib 2021;509:116251.

[6] Li Z, Jiang X, Yin P, Tang L, Wu H, Peng Y, et al. Towards self-powered technique in underwater robots via a high-efficiency electromagnetic transducer with circularly abrupt magnetic flux density change. Appl Energy 2021;302:117569.

[7] Zhang LB, Dai HL, Yang YW, Wang L. Design of high-efficiency electromagnetic energy harvester based on a rolling magnet. Energy Convers Manage 2019;185:202–10.

[8] Halim MA, Cho H, Park JY. Design and experiment of a human-limb driven, frequency up-converted electromagnetic energy harvester. Energy Convers Manage 2015;106:393–404.

[9] Barique MA, Neo Y, Noyori M, Aprila L, Asai M, Mimura H. A large piezoelectric response in highly-aligned electrospun poly(vinylidene fluoride/trifluoroethylene) nanofiber webs for wearable energy harvesting. Nanotechnology 2021;32:015401.

[10] Lu B, Chen Y, Ou D, Chen H, Diao L, Zhang W, et al. Ultra-flexible Piezoelectric Devices Integrated with Heart to Harvest the Biomechanical Energy. Sci Rep 2015;5:16065.

[11] Yuan T-C, Yang J, Chen L-Q. Nonlinear vibration analysis of a circular composite plate harvester via harmonic balance. Acta Mech Sin 2019;35:912–25.

[12] Yuan T-C, Yang J, Chen L-Q. A harmonic balance approach with alternating frequency/time domain progress for piezoelectric mechanical systems. Mech Syst Sig Process 2019;120:274–89.

[13] Li Z, Luo J, Xie S, Xin L, Guo H, Pu H, et al. Instantaneous peak 2.1 W-level hybrid energy harvesting from human motions for self-charging battery-powered electronics. Nano Energy 2021;81:105629.

[14] Qian F, Xu T-B, Zuo L. Design, optimization, modeling and testing of a piezoelectric footwear energy harvester. Energy Convers Manage 2018;171:1352–64.

[15] Qian F, Hajj MR, Zuo L. Bio-inspired bi-stable piezoelectric harvester for broadband vibration energy harvesting. Energy Convers Manage 2020;222:113174.

[16] Yuan T-C, Yang J, Chen L-Q. Nonparametric Identification of Nonlinear Piezoelectric Mechanical Systems. J Appl Mech 2018;85.

[17] Cheng X, Meng B, Zhang X, Han M, Su Z, Zhang H. Wearable electrode-free triboelectric generator for harvesting biomechanical energy. Nano Energy 2015;12:19–25.

[18] Lai Y-C, Deng J, Zhang SL, Niu S, Guo H, Wang ZL. Single-Thread-Based Wearable and Highly Stretchable Triboelectric Nanogenerators and Their Applications in Cloth-Based Self-Powered Human-Interactive and Biomedical Sensing. Adv Funct Mater 2017;27(1):1604462.

[19] Lin Z, Wu Y, He Q, Sun C, Fan E, Zhou Z, et al. An airtight-cavity-structural triboelectric nanogenerator-based insole for high performance biomechanical energy harvesting. Nanoscale 2019;11:6802–9.

[20] Pu X, Li L, Song H, Du C, Zhao Z, Jiang C, et al. A self-charging power unit by integration of a textile triboelectric nanogenerator and a flexible lithium-ion battery for wearable electronics. Adv Mater 2015;27:2472–8.

[21] Wang S, Liu S, Zhou J, Li F, Li J, Cao X, et al. Advanced triboelectric nanogenerator with multi-mode energy harvesting and anti-impact properties for smart glove and wearable e-textile. Nano Energy 2020;78:105291.

[22] Zargari S, Daie Koozehkanani Z, Veladi H, Sobhi J, Rezania A. A new Mylar-based triboelectric energy harvester with an innovative design for mechanical energy harvesting applications. Energy Convers Manage 2021;244:114489.

[23] Erturk A, Inman DJ. Piezoelectric energy harvesting. Chichester: Wiley; 2011.

[24] Kim K-B, Cho JY, Jabbar H, Ahn JH, Hong SD, Woo SB, et al. Optimized composite piezoelectric energy harvesting floor tile for smart home energy management. Energy Convers Manage 2018;171:31–7.

[25] Yuan T, Yang J, Chen L-Q. Nonlinear characteristic of a circular composite plate energy harvester: experiments and simulations. Nonlinear Dyn 2017;90(4):2495–506.

[26] Chen CY, Tsai CY, Xu MH, Wu CT, Huang CY, Lee TH, et al. A fully encapsulated piezoelectric–triboelectric hybrid nanogenerator for energy harvesting from biomechanical and environmental sources. eXPRESS Polym Lett 2019;13:533–42.

[27] Li Z, Saadatnia Z, Yang Z, Naguib H. A hybrid piezoelectric-triboelectric generator for low-frequency and broad-bandwidth energy harvesting. Energy Convers Manage 2018;174:188–97.

[28] Iqbal M, Khan FU, Mehdi M, Cheok Q, Abas E, Nauman MM. Power harvesting footwear based on piezo-electromagnetic hybrid generator for sustainable wearable microelectronics. J King Saud Univers - Eng Sci 2020.

[29] Iqbal M, Khan FU. Hybrid vibration and wind energy harvesting using combined piezoelectric and electromagnetic conversion for bridge health monitoring applications. Energy Convers Manage 2018;172:611–8.

[30] Toyabur RM, Salauddin M, Cho H, Park JY. A multimodal hybrid energy harvester based on piezoelectric-electromagnetic mechanisms for low-frequency ambient vibrations. Energy Convers Manage 2018;168:454–66.

[31] Hamid R, Yuce MR. A wearable energy harvester unit using piezoelectric–electromagnetic hybrid technique. Sens Actuators, A 2017;257:198–207.

[32] Guo Y, Zhang X-S, Wang Y, Gong W, Zhang Q, Wang H, et al. All-fiber hybrid piezoelectric-enhanced triboelectric nanogenerator for wearable gesture monitoring. Nano Energy 2018;48:152–60.

[33] Sun Y, Lu Y, Li X, Yu Z, Zhang S, Sun H, et al. Flexible hybrid piezo/triboelectric energy harvester with high power density workable at elevated temperatures. J Mater Chem A 2020;8:12003–12.

[34] Wu Y, Ma Y, Zheng H, Ramakrishna S. Piezoelectric materials for flexible and wearable electronics: A review. Mater Des 2021;211:110164.

[35] Zhou H, Zhang Y, Qiu Ye, Wu H, Qin W, Liao Y, et al. Stretchable piezoelectric energy harvesters and self-powered sensors for wearable and implantable devices. Biosens Bioelectron 2020;168:112569.

[36] Sezer N, Koç M. A comprehensive review on the state-of-the-art of piezoelectric energy harvesting. Nano Energy 2021;80.

[37] Zhang H, Wen P, Li P, Wang Z, Wang S, Zhao X, et al. Enhanced output performance of flexible piezoelectric energy harvester by using auxetic graphene films as electrodes. Appl Phys Lett 2020;117.

[38] Ji SH, Cho YS, Yun JS. Wearable Core-Shell Piezoelectric Nanofiber Yarns for Body Movement Energy Harvesting. Nanomaterials (Basel) 2019;9.

[39] Waseem A, Johar MA, Hassan MA, Bagal IV, Ha J-S, Lee JK, et al. GaN/Al2O3 core-shell nanowire based flexible and stable piezoelectric energy harvester. J Alloy Compd 2021;860.

[40] Wang Q, Kim K-B, Woo SB, Song YS, Sung TH. A Flexible Piezoelectric Energy Harvester-Based Single-Layer WS2 Nanometer 2D Material for Self-Powered Sensors. Energies 2021;14.

[41] Mokhtari F, Shamshirsaz M, Latifi M, Foroughi J. Nanofibers-Based Piezoelectric Energy Harvester for Self-Powered Wearable Technologies. Polymers (Basel) 2020;12.

[42] Zhong J, Zhong Q, Zang X, Wu N, Li W, Chu Y, et al. Flexible PET/EVA-based piezoelectret generator for energy harvesting in harsh environments. Nano Energy 2017;37:268–74.

[43] Meschino M, Wang L, Xu H, Moradi-Dastjerdi R, Behdinan K. Low-frequency nanocomposite piezoelectric energy harvester with embedded zinc oxide nanowires. Polym Compos 2021;42:4573–85.

[44] Kim J, Byun S, Lee S, Ryu J, Cho S, Oh C, et al. Cost-effective and strongly integrated fabric-based wearable piezoelectric energy harvester. Nano Energy 2020;75.

[45] Han R, Zheng L, Li G, Chen G, Ma S, Cai S, et al. Self-Poled Poly(vinylidene fluoride)/MXene Piezoelectric Energy Harvester with Boosted Power Generation Ability and the Roles of Crystalline Orientation and Polarized Interfaces. ACS Appl Mater Interfaces 2021;13:46738–48.

[46] Wang C, Wang S, Gao Z, Wang X. Applicability evaluation of embedded piezoelectric energy harvester applied in pavement structures. Appl Energy 2019;251.

[47] Qian, F. Xu, T.-B. Zuo, L.J.Ec. management. Design, optimization, modeling and testing of a piezoelectric footwear energy harvester. 171 (2018) 1352-64.

[48] Wang, C. Wang, S. Li, Q.J. Wang, X. Gao, Z. Zhang, L.J.E.C.et al. Fabrication and performance of a power generation device based on stacked piezoelectric energy-harvesting units for pavements. 163 (2018) 196-207.

[49] Qian, F. Xu, T.-B. Zuo, L.J.S.M. Structures. Material equivalence, modeling and experimental validation of a piezoelectric boot energy harvester. 28 (2019) 075018.

[50] Wu Z, Xu Q. Design and testing of a new dual-axial underfloor piezoelectric energy harvester. Sens Actuators, A 2020;303.

[51] Khalili M, Biten AB, Vishwakarma G, Ahmed S, Papagiannakis AT. Electro-mechanical characterization of a piezoelectric energy harvester. Appl Energy 2019;253.

[52] Lynch, J.P. Chen, S. Wang, L. Zhou, W. Musgrave, P. Xu, T.-B. et al. Optimal design of force magnification frame of a piezoelectric stack energy harvester. Sensors and Smart Structures Technologies for Civil, Mechanical, and Aerospace Systems 20152015.

[53] Zhou S, Zuo L. Nonlinear dynamic analysis of asymmetric tristable energy harvesters for enhanced energy harvesting. Commun Nonlinear Sci Numer Simul 2018;61:271–84.

[54] Yuan T-C, Yang J, Chen L-Q. Nonlinear dynamics of a circular piezoelectric plate for vibratory energy harvesting. Commun Nonlinear Sci Numer Simul 2018;59:651–6.

[55] Yan B, Wang Z, Ma H, Bao H, Wang K, Wu C. A novel lever-type vibration isolator with eddy current damping. J Sound Vib 2021;494.

[56] Fang S, Wang S, Miao G, Zhou S, Yang Z, Mei X, et al. Comprehensive theoretical and experimental investigation of the rotational impact energy harvester with the centrifugal softening effect. Nonlinear Dyn 2020;101:123–52.

[57] Huang D, Chen J, Zhou S, Fang X, Li W. Response regimes of nonlinear energy harvesters with a resistor-inductor resonant circuit by complexification-averaging method. Sci China Technol Sci 2021;64:1212–27.

[58] Dechant, E. Fedulov, F. Chashin, D.V. Fetisov, L.Y. Fetisov, Y.K. Shamonin, M.J.S. M. et al. Low-frequency, broadband vibration energy harvester using coupled oscillators and frequency up-conversion by mechanical stoppers. 26 (2017) 065021.

[59] Hu G, Tang L, Das R. An impact-engaged two-degrees-of-freedom Piezoelectric Energy Harvester for Wideband Operation. Procedia Eng 2017;173:1463–70.

[60] Wen S, Xu Q. Design of a Novel Piezoelectric Energy Harvester Based on Integrated Multistage Force Amplification Frame. IEEE/ASME Trans Mechatron 2019;24:1228–37.

[61] Wu Z, Xu Q. Design and Development of a Novel Two-Directional Energy Harvester With Single Piezoelectric Stack. IEEE Trans Ind Electron 2021;68:1290–8.

[62] Kim, H. Priya, S. Stephanou, H. Uchino, K.J.I.t.o.u. ferroelectrics, f. control. Consideration of impedance matching techniques for efficient piezoelectric energy harvesting. 54 (2007) 1851-9.

[63] Kuang, Y. Yang, Z. Zhu, M.J.S.M. Structures. Design and characterisation of a piezoelectric knee-joint energy harvester with frequency up-conversion through magnetic plucking. 25 (2016) 085029.